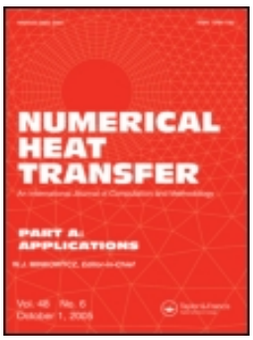

Taylor & Francis
Taylor & Francis Group

Numerical Heat Transfer, Part A: Applications

ISSN: 1040-7782 (Print) 1521-0634 (Online) Journal homepage: https://www.tandfonline.com/loi/unht20

Natural Convection in a Rectangular Cavity Heated from Below and Uniformly Cooled from the Top and Both Sides

Amaresh Dalal & Manab Kumar Das

To cite this article: Amaresh Dalal & Manab Kumar Das (2006) Natural Convection in a Rectangular Cavity Heated from Below and Uniformly Cooled from the Top and Both Sides, Numerical Heat Transfer, Part A: Applications, 49:3, 301-322

To link to this article: https://doi.org/10.1080/10407780500343749

Published online: 15 Aug 2006.

Numerical Heat Transfer, Part A, 49: 301–322, 2006

ISSN: 1040-7782 print/1521-0634 online
DOI: 10.1080/10407780500343749

Taylor & Francis
Taylor & Francis Group

NATURAL CONVECTION IN A RECTANGULAR CAVITY HEATED FROM BELOW AND UNIFORMLY COOLED FROM THE TOP AND BOTH SIDES

Amaresh Dalal
Department of Mechanical Engineering, Indian Institute of Technology Kanpur, Kanpur, India

Manab Kumar Das
Department of Mechanical Engineering, Indian Institute of Technology Guwahati, Guwahati, India

In this article, a study of natural convection inside a rectangular cavity is carried out. The bottom wall is heated by a spatially varying temperature and other three walls are kept constant at lower temperature. The integral forms of the governing equations are solved numerically using the finite-volume method in a nonorthogonal body-fitted coordinate system. The SIMPLE algorithm with higher-order upwinding scheme is used. Results are presented in the form of local and average Nusselt number distribution for a range of Rayleigh numbers (10^0–10^6) and aspect ratios (0.5, 0.75, 1, 1.25, 1.5, and 2). The streamlines and isothermal lines are presented for various Rayleigh numbers and a fluid having Prandtl number 0.71.

INTRODUCTION

The natural-convection process has received considerable importance over the past years because of its relevance to heat transfer in many science and engineering applications. Numerous references deal with enclosures with flat walls, due to its relevance to large-scale natural phenomena in the fields of astrophysics, geophysics, atmospheric sciences, and a wide range of engineering applications such as cooling of electronic equipment, solidification processes, growing crystals, and solar collectors. There are always complex interactions between the finite fluid content inside the enclosure and the enclosure walls. Since the velocity and the temperature equations are coupled due to the buoyancy force, the study of natural convection is very complex.

A large number of articles available in the literature deal with the study of natural convection in simple-geometry enclosures with either vertical or horizontal imposed heat flux or temperature difference. A thorough review is given by

Received 24 May 2005; accepted 17 August 2005.
Amaresh Dalal acknowledges the computation facilities extended by the CFD Laboratory of the Mechanical Engineering Department, IIT Kanpur.
Address correspondence to Manab Kumar Das, Department of Mechanical Engineering, Indian Institute of Technology, North Guwahati, Guwahati, Assam 781039, India. E-mail: manab@iitg.ernet.in

NOMENCLATURE

A	aspect ratio ($= H/L$)
g	gravitational acceleration
H	height of the enclosure
J	Jacobian
L	length of the enclosure
Nu	Nusselt number
p	dimensionless pressure
Pr	Prandtl number
P, Q	grid control functions
q_1, q_2, q_3	geometric relations between coordinate systems
Ra	Rayleigh number
S	source term
T	dimensionless temperature
ΔT	differential temperature, dimensionless
u, v	dimensionless velocity components in x and y directions
U, V	dimensionless contravariant velocity components in ξ and η directions
x, y	dimensionless Cartesian coordinates
α	thermal diffusivity
ξ, η	dimensionless curvilinear coordinates
ϕ	general variable representing u, v, and T
ψ	streamfunction

Subscripts

av	average
c	cold wall
h	hot wall
l	local
max	maximum
x, y, ξ, η	derivatives relative to x, y, ξ, η, respectively

Superscript

*	dimensional form

Ostrach [1]. Though many different boundary conditions are considered in practice, rather little work has been carried out for more complex boundary conditions, for example, when the assigned gradient is neither simply horizontal or vertical. Oosthuizen [2] has considered a case with heating from the bottom surface and cooling from the top surface. The side walls are maintained at a linearly varying temperature. This type of problem is encountered in the crop drying process. A parametric study has been done by varying Ra, Pr, and the aspect ratio. Oosthuizen and Monaghan [3] have considered a nonrectangular cavity in which the bottom is a hot surface and the enclosure is being cooled from the top. The side walls have linearly varying temperature. In another study, Oosthuizen [4] considered cooling from the top surface when the heating is taking place from the bottom surface. Part of the side walls are maintained at cold temperature and part vary with a linear profile. A rectangular enclosure heated from below and symmetrically cooled from the sides was analyzed by Ganzarolli and Milanez [5]. The top surface was maintained at adiabatic condition. The range of Ra considered was $10^3 - 10^7$. The aspect ratio (length/height) was varied from 1 to 9 and Pr = 0.7 and 7 were considered. A single cell was observed to represent the flow pattern. Chmaissem and Daguenet [6] studied the heat transfer process when the cavity is maintained at hot and cold condition on the opposite walls. The effects of the geometry and Ra on the flow and isotherm pattern were studied. Kumar et al. [7] studied the transition from laminar to chaotic natural-convection flow in a unity-aspect-ratio rectangular cavity with mixed thermal boundary conditions. They reported critical Rayleigh number for the onset of transition and finally leading to various measures of chaos.

Aydin et al. [8] considered heating from one side and cooling from the top while two other walls were maintained at adiabatic condition. The effect of Ra and

the aspect ratio on the flow pattern and energy transport were investigated. Sezai and Mohamad [9] studied natural convection in a rectangular cavity heated from below and cooled from all other sides. The occurrence and structure of the different flow patterns were examined for $\mathrm{Ra} \leq 10^4$ in an enclosure having an aspect ratio of 4 and a square horizontal cross section. Sarris et al. [10] studied the effect of heat transfer in a square enclosure by natural convection with periodic heating from above over the entire top wall and adiabatic bottom and side-wall boundary conditions. They solved the problem numerically for regular geometry for higher Prandtl number ($\mathrm{Pr} = 100$). The value of Rayleigh number was varied from 10^3 to 10^8. Recently, Dalal and Das [11] considered a case of heating from the top surface with a sinusoidally varying temperature and cooling from the other three surfaces The right vertical surface was undulated, having one and three numbers of undulations. The effect of the number and the amplitude of undulation was studied. In another study, Dalal and Das [12] made a detailed study by considering the same geometry as [11]. Additionally, they considered the effect of angle of inclination.

The literature survey shows that heating from the bottom by a sinusoidally varying temperature and cooling simultaneously from the other three walls has not been considered so far. In the present investigation, a numerical analysis of natural convection in a rectangular cavity heated from below and symmetrically cooled from the top and both sides is considered. The two vertical and top walls are cooled with a fixed temperature, whereas the bottom wall is heated with a sinusoidal temperature distribution in space coordinates. Air is taken as the working fluid, with $\mathrm{Pr} = 0.71$. The flow structure type and heat transfer rate are analyzed and discussed for a wide range of Rayleigh numbers (10^0 to 10^6) and aspect ratios (0.5, 0.75, 1.0, 1.25, 1.5, and 2.0).

PROBLEM SPECIFICATION

Figure 1*a* shows the geometry of the two-dimensional square cavity filled with viscous fluid. The bottom wall temperature is considered to be spatially varying with sinusoidal temperature distribution, $T_h^*(x^*)$. The other three walls are considered to be of constant temperature, T_c^*. The temperature distribution on the bottom wall is [10]

$$T_h^*(x^*) = T_c^* + \frac{\Delta T^*}{2}\left[1 - \cos\left(\frac{2\pi x^*}{L}\right)\right] \tag{1}$$

where T_c^* is the minimum value of the imposed temperature distribution and ΔT^* is the temperature difference between the maximum and the minimum temperatures of the bottom wall. Equation (1) can be written in dimensionless form as follows and shown in Figure 1*b*:

$$T_h(x) = \frac{1}{2}[1 - \cos(2\pi x)] \tag{2}$$

The fluid considered in this study is air ($\mathrm{Pr} = 0.71$). The Rayleigh number is varied from 10^0 to 10^6.

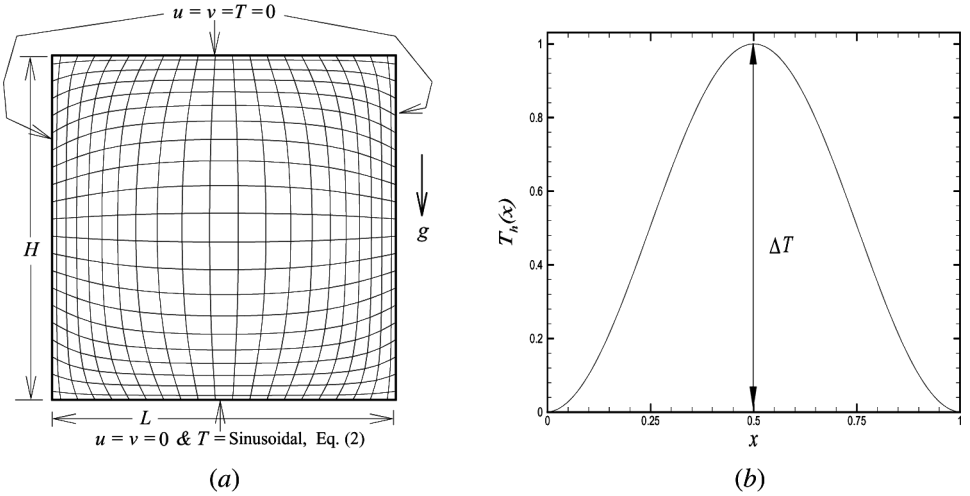

Figure 1. (*a*) Computational domain and boundary conditions. (*b*) Sinusoidal temperature distribution at bottom wall.

GOVERNING EQUATIONS AND BOUNDARY CONDITIONS

Natural convection is governed by differential equations expressing the conservation of mass, momentum, and energy. The present flow is considered steady, laminar, incompressible, and two-dimensional. The viscous dissipation term in the energy equation is neglected. The variation of fluid properties with temperature is also neglected, except for the buoyancy term, for which the Boussinesq approximation is adopted. The governing equations and the boundary conditions are cast in dimensionless form using the following dimensionless variables:

$$x = \frac{x^*}{L} \quad y = \frac{y^*}{L} \quad u = \frac{u^* L}{\alpha} \quad v = \frac{v^* L}{\alpha} \quad p = \frac{p^* L^2}{\rho \alpha^2} \quad T = \frac{T^* - T_c^*}{\Delta T^*} \tag{3}$$

The resulting equations are as follows.
Continuity equation:

$$\frac{\partial u}{\partial x} + \frac{\partial v}{\partial y} = 0 \tag{4}$$

u-momentum equation:

$$\frac{\partial (u^2)}{\partial x} + \frac{\partial (uv)}{\partial y} = -\frac{\partial p}{\partial x} + \mathrm{Pr}\left(\frac{\partial^2 u}{\partial x^2} + \frac{\partial^2 u}{\partial y^2}\right) \tag{5}$$

v-momentum equation:

$$\frac{\partial (uv)}{\partial x} + \frac{\partial \left(v^2\right)}{\partial y} = -\frac{\partial p}{\partial y} + \mathrm{Pr}\left(\frac{\partial^2 v}{\partial x^2} + \frac{\partial^2 v}{\partial y^2}\right) + \mathrm{Ra}\ \mathrm{Pr}\ T \tag{6}$$

Energy equation:

$$\frac{\partial(uT)}{\partial x}+\frac{\partial(vT)}{\partial y}=\frac{\partial^2 T}{\partial x^2}+\frac{\partial^2 T}{\partial y^2} \tag{7}$$

In addition, the velocity and temperature boundary conditions take the following forms:

$$\begin{aligned} &u=v=T=0 && \text{for } x=0,1 \text{ and } 0\le y\le 1\\ &u=v=T=0 && \text{for } y=1 \text{ and } 0\le x\le 1\\ &u=v=0 \text{ and } T=\frac{1}{2}[1-\cos(2\pi x)] && \text{for } y=0 \text{ and } 0\le x\le 1 \end{aligned} \tag{8}$$

TRANSFORMATION OF THE GOVERNING EQUATIONS

The governing equations transformed from the Cartesian system (x, y) to the boundary-fitted coordinate system (ξ, η) [13, 14] are given by the following.
Continuity equation:

$$U_\xi + V_\eta = 0 \tag{9}$$

Generalized momentum and energy equations:

$$(U\phi)_\xi + (V\phi)_\eta = S(\xi,\eta) + \left[\frac{\Gamma}{J}(q_1\,\phi_\xi - q_2\,\phi_\eta)\right]_\xi + \left[\frac{\Gamma}{J}(-q_2\,\phi_\xi + q_3\,\phi_\eta)\right]_\eta \tag{10}$$

where $\Gamma = \mathrm{Pr}$ for the momentum equation and $\Gamma = 1$ for the energy equation. The source term $S(\xi, \eta)$ is given by

$$\begin{aligned} &S(\xi,\eta) = -y_\eta p_\xi + y_\xi p_\eta && \text{for } \phi = u\\ &S(\xi,\eta) = x_\eta p_\xi - x_\xi p_\eta + J\ \mathrm{Ra}\ \mathrm{Pr}\ T && \text{for } \phi = v\\ &S(\xi,\eta) = 0 && \text{for } \phi = T \end{aligned} \tag{11}$$

The expressions for $q_1,\ q_2,\ q_3$, and J are given in Eq. (21). The relationships between the Cartesian and contravariant velocity components are

$$U = y_\eta u - x_\eta v \qquad V = x_\xi v - y_\xi u \tag{12}$$

The boundary condition given in Eq. (8) are Dirichlet type. The boundary condition for computational plane can be written as follows:

$$\begin{aligned} &u=v=T=0 && \text{for } \xi=0,1 \text{ and } 0\le \eta\le 1\\ &u=v=T=0 && \text{for } \eta=1 \text{ and } 0\le \xi\le 1\\ &u=v=0 \text{ and } T=\frac{1}{2}[1-\cos(2\pi x)] && \text{for } \eta=0 \text{ and } 0\le \xi\le 1 \end{aligned} \tag{13}$$

The heat transfer rate by convection in an enclosure is obtained from the Nusselt number calculation. The local Nusselt numbers in different walls are expressed as

$$\begin{aligned}
\text{Top wall:} \quad & \mathrm{Nu}_l = \frac{1}{J\sqrt{q_3}}(q_3 T_\eta - q_2 T_\xi) \\
\text{Right wall:} \quad & \mathrm{Nu}_l = \frac{1}{J\sqrt{q_1}}(q_1 T_\xi - q_2 T_\eta) \\
\text{Bottom wall:} \quad & \mathrm{Nu}_l = \frac{-1}{J\sqrt{q_3}}(q_3 T_\eta - q_2 T_\xi) \\
\text{Left wall:} \quad & \mathrm{Nu}_l = \frac{-1}{J\sqrt{q_1}}(q_1 T_\xi - q_2 T_\eta)
\end{aligned} \tag{14}$$

The average Nusselt number is calculated by

$$\mathrm{Nu}_{\mathrm{av}} = \frac{1}{L}\int_0^L \mathrm{Nu}_l \, dl$$

GRID GENERATION

Numerical grid generation has now become a fairly common tool for use in the numerical solution of partial differential equations on arbitrarily shaped regions. The coordinate transformation technique advanced by Thompson et al. [15] is used for the solution of problems over complex geometries. The transformation is obtained from the solution of partial differential equations on the regular computational domain. Mapping is done to convert the regions having irregular shape (physical domain) into the computational domain, where the geometry becomes regular with a suitable transformation. A curvilinear mesh is generated over the physical domain such that one member of each family of curvilinear coordinate lines is coincident with the boundary contour of the physical domain [14]. The Navier–Stokes equations are then solved on the transformed plane and the solution is back-transformed to the physical plane. The transformation is

$$\xi \equiv \xi(x, y) \qquad \eta \equiv \eta(x, y) \tag{15}$$

and the inverse transformation is given by

$$x \equiv x(\xi, \eta) \qquad y \equiv y(\xi, \eta) \tag{16}$$

The mapping to the body-fitted coordinate system is constructed by specifying the desired points (x, y) on the boundary of the physical domain. The distribution of points on the interior is determined by solving a system of Poisson equations:

$$\xi_{xx} + \xi_{yy} = P(\xi, \eta) \tag{17}$$

$$\eta_{xx} + \eta_{yy} = Q(\xi, \eta) \tag{18}$$

Equations (17) and (18) are then transformed to computational space by interchanging the roles of the independent and dependent variables. This yields a system of two equations of the form

$$q_1\, x_{\xi\xi} - 2\, q_2\, x_{\xi\eta} + q_3\, x_{\eta\eta} + J^2(P\, x_\xi + Q\, x_\eta) = 0 \tag{19}$$

$$q_1\, y_{\xi\xi} - 2\, q_2\, y_{\xi\eta} + q_3\, y_{\eta\eta} + J^2(P\, y_\xi + Q\, y_\eta) = 0 \tag{20}$$

where the geometric coefficients $q_1,\ q_2,\ q_3$ and the Jacobian J are given by

$$\begin{aligned} q_1 &= x_\eta^2 + y_\eta^2 \\ q_2 &= x_\xi\, x_\eta + y_\xi\, y_\eta \\ q_3 &= x_\xi^2 + y_\xi^2 \\ J &= x_\xi\, y_\eta - x_\eta\, y_\xi \end{aligned} \tag{21}$$

P and Q are functions that provide control of the mesh concentration. The values of P and Q have to be chosen depending on the clustering of the grid required for the problem in hand. The transformed equations (19) and (20) are discretized over the computational plane using second-order differencing and then solved numerically. The coefficients in Eq. (21) are computed at each grid point.

NUMERICAL PROCEDURE

A code has been developed to solve the governing equations in the nonorthogonal coordinate system based on the transformation from physical domain to the computational domain (Dalal [16]). Further, the code has been applied to natural-convection problems in nonregular geometries (Dalal and Das [11, 12]). Here, though the geometry is regular (rectangular), the same developed and tested code has been used to solve the problem.

Equations (9) and (10) are discretized using staggered, nonuniform control volumes, and these equations are solved numerically by finite-volume method. A typical control volume, in both Cartesian and curvilinear coordinates, is shown in Figure 2. The semi-implicit method for pressure-linked equation (SIMPLE) [17] is used to couple momentum and continuity equations. In order to minimize the numerical diffusion errors, the deferred QUICK scheme of Hayase et al. [18] is employed in approximating the convective terms for both the momentum equations and the energy equation. The central difference scheme is employed near the boundary points for the convective terms. Tri diagonal matrix algorithm (TDMA) [17] is applied for the line-by-line solution of the momentum, energy, and pressure-correction equations. The pseudo-transient approach is followed for the numerical solution, as it is useful for situations in which governing equations give rise to stability problems, e.g., buoyant flows [19]. An underrelaxation factor for pressure with a value of 0.01 is used, and the pseudo-time step is taken as 10^{-2} for $\mathrm{Ra} = 10^0 - 10^2; 10^{-3}$ for $\mathrm{Ra} = 10^3, 10^4; 10^{-4}$ for $\mathrm{Ra} = 10^5$; and 10^{-5} for $\mathrm{Ra} = 10^6$.

The iterative procedure is initiated by solution of the energy equation followed by the momentum equations and is continued until convergence is achieved. The

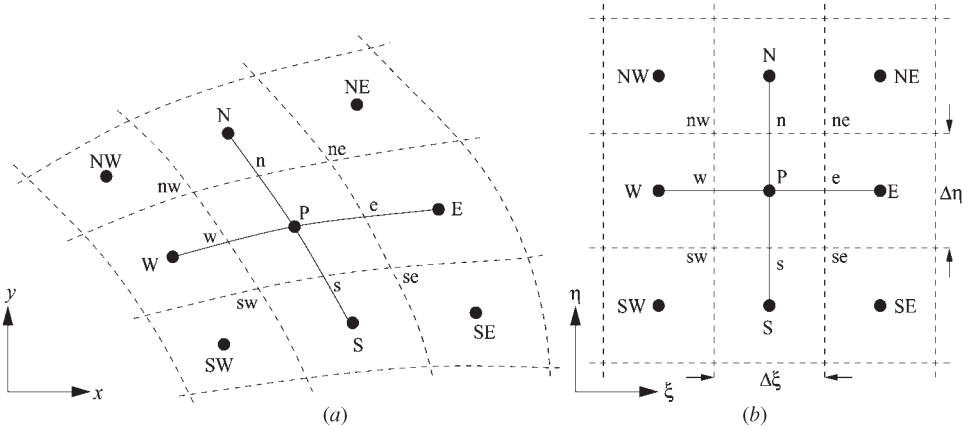

Figure 2. A typical 2-D control volume and the notation used.

Euclidean norm of the residual is taken as convergence criterion for each dependent variable in the entire flow field [20]. The mass balance for global convergence is taken as 10^{-8}.

CODE VALIDATION

The present code is validated with the numerical results of de Vahl Davis [21], Markatos and Perikleous [22], and Hadjisophocleous et al. [23] for the buoyancy-driven laminar heat transfer in a square cavity with differentially heated side walls. The left wall is kept hot while the right wall is cooled. The top and bottom walls are insulated.

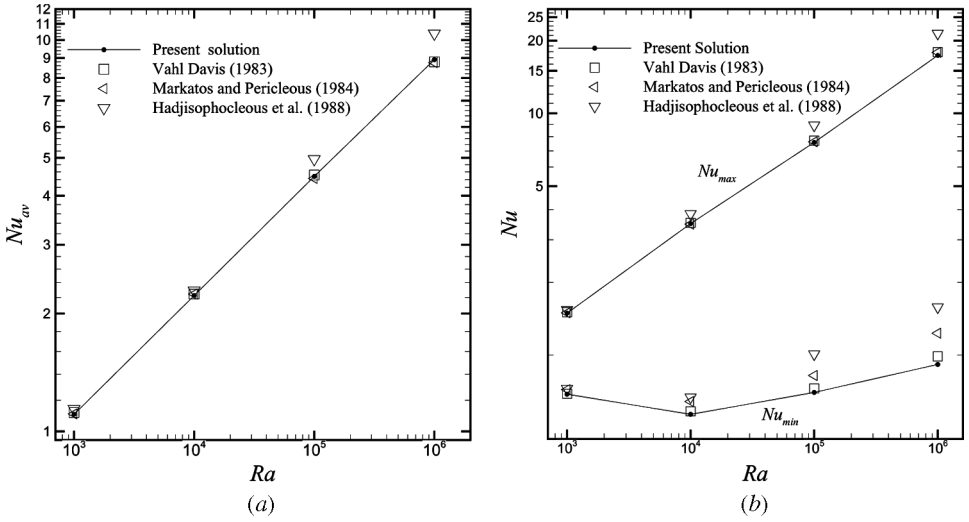

Figure 3. (*a*) Comparison of Nu_{av} on hot wall. (*b*) Comparison of Nu_{max} and Nu_{min} on hot wall.

In the present work, numerical predictions using the algorithm developed have been obtained for Rayleigh numbers between 10^3 and 10^6 on an elliptic mesh with 61×61 grid points. Figure 3*a* shows the comparison of average Nusselt number on the hot wall. Comparison of maximum and minimum Nusselt numbers on the hot wall is shown in Figure 3*b*. Comparison of the results is also given by Dalal and Das [11, 12]. The results are in very good agreement with the benchmark solution.

GRID INDEPENDENCE STUDY

The grid independence test is performed for the square cavity ($A = 1$) using successively sized grids, 21×21 to 141×141, with an increment of 20 for $\mathrm{Ra} = 10^5$ and $A = 1$. Figure 4 shows the maximum streamfunction for various grid sizes. It is observed that there is very small change of $\psi_{\max}$ for 121×121 and 141×141. Table 1 shows that there is 1.48% change in $\mathrm{Nu}_{\mathrm{av}}$ on the bottom wall from 101×101 to 121×121, whereas the difference is 0.78% from 121×121 to 141×141. Based on this observation, grid size of 121×121 is used for further calculations for $A = 1$. Grid sizes of 121×61, 121×91, 121×121, 121×121, and 121×121 are used for all of the calculations for $A = 0.5$, 0.75, 1.25, 1.5, and 2, respectively. The point to be noted here is that for $A = 1.25$, 1.5, and

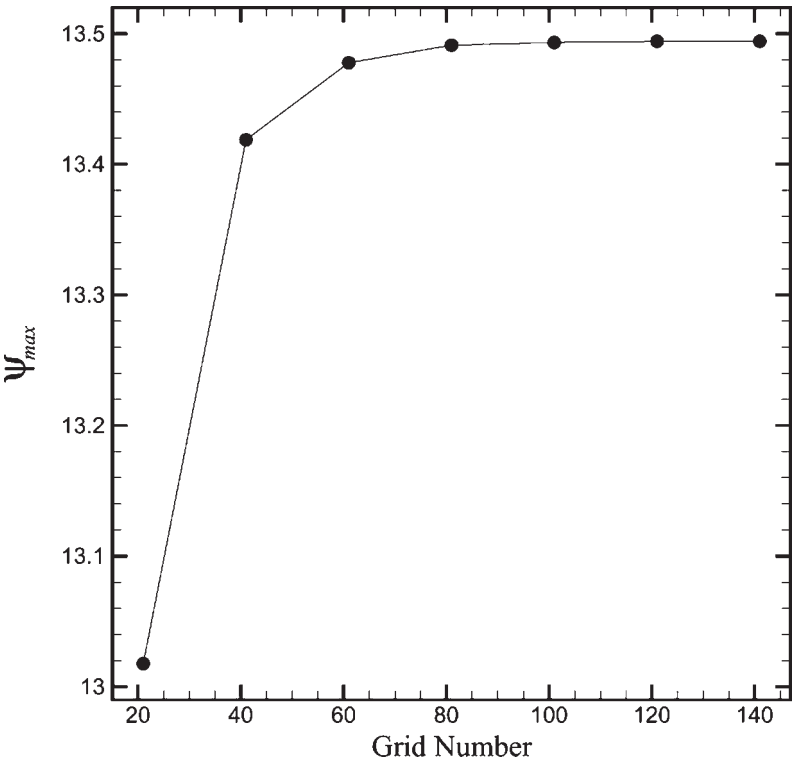

Figure 4. Grid independence test for $\mathrm{Ra} = 10^5$ and $A = 1$.

Table 1. Nu_{av} for $A = 1$

Grid size	Right wall	Bottom wall	Top wall
101×101	-1.056319	4.270104	-2.057704
121×121	-1.051330	4.220680	-2.042751
141×141	-1.047754	4.187696	-2.032529

2.0, we have used grid numbers of 121×121 because the time required for the mass residual to fall below 10^{-8} is enormous.

RESULTS AND DISCUSSION

Flow and temperature fields and heat transfer rates are examined for ranges of Ra (10^0–10^6), A(0.5, 0.75, 1, 1.25, 1.5, and 2), and Pr = 0.71. The discussion of the following results concerns the temperatures, streamlines, local Nusselt number distributions, and average Nusselt number on the walls. The streamfunction and temperature distribution for $Ra = 10^5$ and $A = 1$ are shown in Figures 5*a* and 5*b*, respectively. A pair of counterrotating cells is formed in the left and right halves of the enclosure (Figure 5*a*). The resulting flow patterns and temperature fields are symmetric with respect to a vertical plane passing through the center of the bottom wall. So, for brevity, the streamlines and the isothermal lines are shown in the left half and right half, respectively, in further plots.

Figures 6*a*–6*d* show the streamlines and the isothermal lines for $Ra = 10^3 - 10^6$ and $A = 1$. There is not much variation in flow patterns for $Ra = 10^0 - 10^3$, so the streamlines and isothermal lines are shown from $Ra = 10^3$

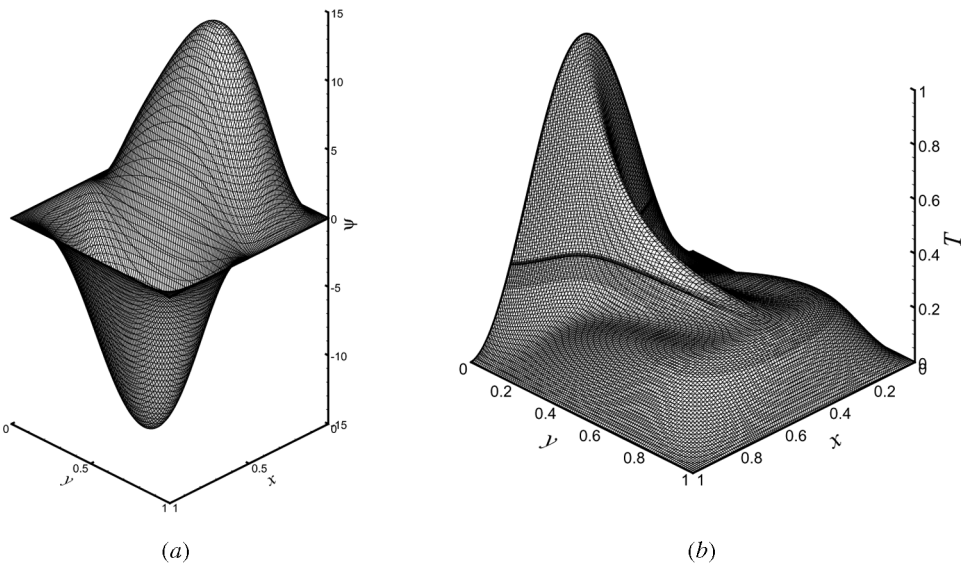

Figure 5. Streamfunction and temperature distribution for $Ra = 10^5$.

onwards. The fluid after being heated from the bottom wall moves up near the vertical midplane of the enclosure. Then the fluid impinges near the middle of the top wall and moves horizontally toward the corners, losing heat to the top wall. Finally, it descends along the cold side walls. For lower Ra (10^3 and 10^4), the isothermal lines are uniformly distributed inside the cavity, as conduction is the main heat transfer mechanism in this case. The isothermal lines swirl at $\mathrm{Ra} = 10^5$ due to the influence of the convection current. It is observed from Table 2 that the intensity of the recirculation pattern increases with increase of Ra. Maximum streamfunction value occurs at the center of the cells. It is observed that up to $\mathrm{Ra} = 10^3$, $\psi_{\max}$ values remain relatively small, implying that the convection velocity

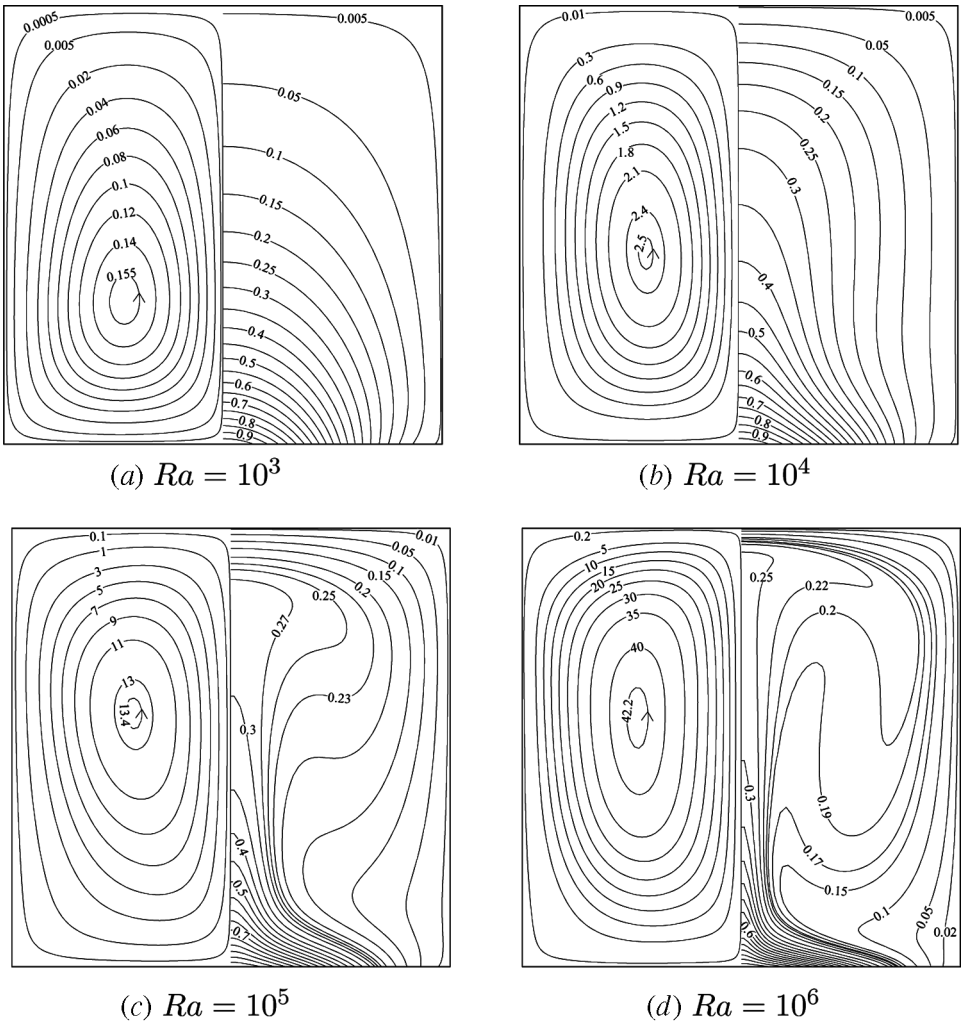

Figure 6. Streamlines and isothermal lines for $A = 1$.

Table 2. Comparison of ψ_{max} for $A = 1$

Ra	ψ_{max}	x	y
10^0	0.000146	0.272174	0.319216
10^1	0.001428	0.272994	0.308033
10^2	0.014860	0.272174	0.319216
10^3	0.159580	0.271413	0.330612
10^4	2.519170	0.288129	0.440401
10^5	13.494199	0.277759	0.572123
10^6	42.572238	0.267396	0.571587

is also small. The center of the cell remains unaltered. However, with increase of Ra, the ψ_{max} values increase drastically, with a considerable shift of the center of the cell in the positive y direction. The horizontal centerline temperature and streamfunction distribution are shown in Figures 7*a* and 7*b*. A close inspection reveals that the temperature profiles for $Ra = 10^3$ and 10^4 closely resemble the shape of the imposed temperature profile on the hot bottom surface. For $Ra = 10^5$, a short uniform core region is developed for the right and left cells. As the Ra is increased ($= 10^6$), the uniform core region increases, implying that better mixing due to increased convection is achieved. The maximum horizontal temperature value (i.e., the value of T at the center of the cavity) increases from $Ra = 10^3$ to $Ra = 10^4$ and then decreases with increase of Ra for the same reason. The streamfunction plot in the horizontal midheight plane ($y = 0.5$) also confirms that the convection velocity increases markedly with increase of Ra, and all the curves pass through a ψ value at $x = 0.5$.

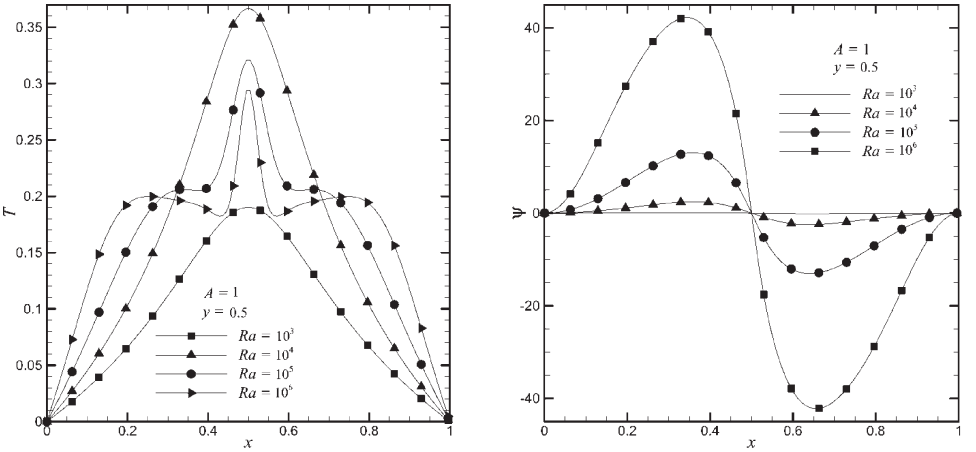

Figure 7. (*a*) Temperature profile. (*b*) Streamfunction profile in horizontal centerline.

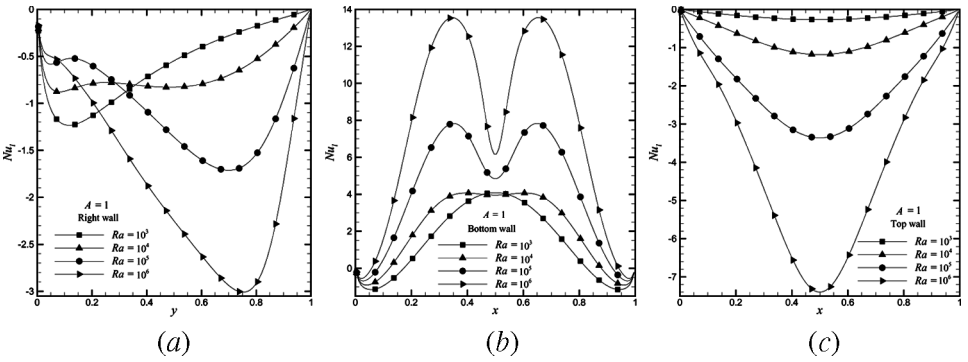

Figure 8. Local Nusselt number distribution.

The local Nusselt number distribution in the right, bottom, and top walls is shown in Figures 8*a*, 8*b*, and 8*c*, respectively, for the Rayleigh number studied. The peak point of maximum heat rejection (negative $\mathrm{Nu}_{\max}$) from the fluid to the right wall gradually shifts from bottom to top with increase of the Rayleigh number (Figure 8*a*). This is because, with increase of Ra, a wall jet of fluid is formed on the top middle region. It impinges on the right (or left) vertical top corner and takes a bend down the vertical wall. Thus the maximum Nu_l value is undergoing a shift in the positive y direction and Ra is increased. Figure 8*b* shows that, for higher Rayleigh number, the isothermal lines are concentrated near the bottom wall and thus the heat transfer rate is greater in magnitude. Close to $x = 0$ and 1, Nu_l has a negative value, which means that there is heat rejection from the hot wall instead of heat addition to the enclosure. This is due to the higher temperature of the downward fluid compared to the sinusoidally varying temperature. For the higher Rayleigh numbers, the recirculation intensity increases (Table 2) and the isothermal lines are concentrated near the middle region of the top wall, which produces a peak in the local Nusselt number near the middle region of the top wall of the enclosure (Figure 8*c*). It is interesting to note that the Nu_l distribution resembles a near-cosine distribution for a sinusoidally varying bottom wall temperature. The absolute $\mathrm{Nu}_{\max}$ on the right wall for various Ra is shown in Table 3. Up to $\mathrm{Ra} = 10^3$, $\mathrm{Nu}_{\max}$ remains constant and occurs at the same y location. However, for $\mathrm{Ra} = 10^4$, it decreases

Table 3. Comparison of $\mathrm{Nu}_{\max}$ on the right wall for $A = 1$

Ra	$\mathrm{Nu}_{\max}$	y
10^0	–1.263812	0.112500
10^1	–1.256103	0.112500
10^2	–1.263383	0.112500
10^3	–1.232699	0.120833
10^4	–0.878886	0.079167
10^5	–1.712428	0.695833
10^6	–3.010422	0.754167

Table 4. Comparison of Nu_{max} on the bottom wall for $A = 1$

Ra	Nu_{max}	x
10^0	4.182631	0.5
10^1	4.202738	0.5
10^2	4.168408	0.5
10^3	4.092390	0.5
10^4	4.073659	0.395833, 1–0.395833
10^5	7.830753	0.354167, 1–0.354167
10^6	13.553487	0.345833, 1–0.345833

(–0.88) with lowering of the the location (0.08). Then for $Ra = 10^5$, it suddenly increases (–1.71) and occurs at $y = 0.696$. With further increase of Ra, the trend continues. This clearly shows the effect of convection on the flow and heat transfer. The magnitude of Nu_{max} and the location on the bottom wall for various Ra are given in Table 4. Up to $Ra = 10^3$, Nu_{max} remains constant and occurs at $x = 0.5$. With increase of Ra, it occurs at two locations, one at the left cell and another on the right cell, and they are symmetrical.

Streamlines and isothermal lines for $A = 0.5, 0.75, 1.25, 1.5,$ and 2 are shown in Figures 9–13, respectively, for various Rayleigh number. A qualitative comparison by visual inspection reveals that for all the aspect ratios considered, conduction dominates up to $Ra = 10^3$. After that, kinks due to the relatively comparable

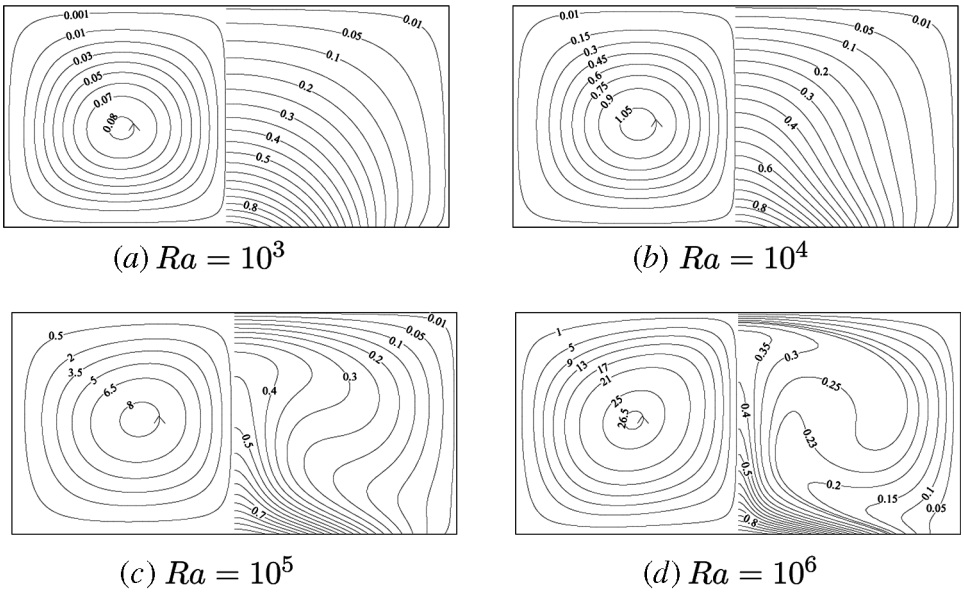

Figure 9. Streamlines and isothermal lines for $A = 0.5$.

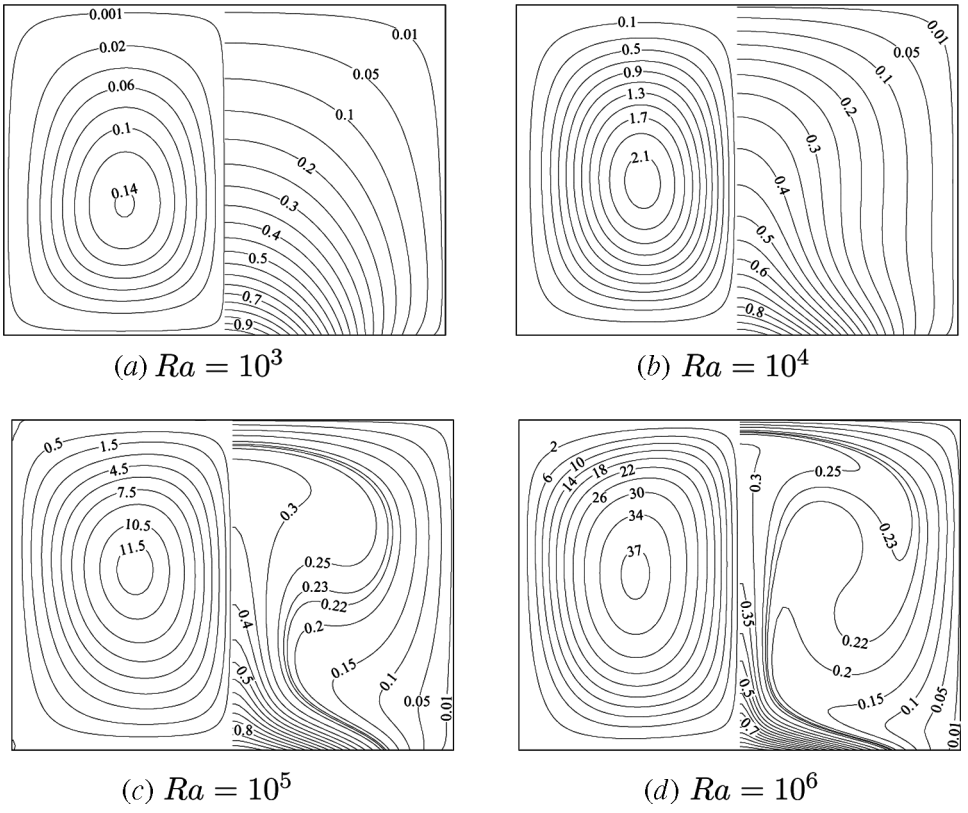

Figure 10. Streamlines and isothermal lines for $A = 0.75$.

magnitude of convection appear in the isotherm patterns. Thus it may be said that there is a shift from conduction to convection mode of heat transfer in this region. The flow remains steady, with one rotating cell in each of the halves (left or right). Figures 14*a* and 14*b* show the horizontal centerline temperature and streamfunction distribution for $\mathrm{Ra} = 10^6$ and various aspect ratios. With increase of aspect ratio, the maximum temperature decreases. Also, the spread of the core with approximately uniform temperature decreases. As the height of the enclosure increases, the combined diffusion and convection effect does not penetrate deep into the cavity and thus the temperature decreases. The streamfunction value increases with aspect ratio (Figure 14*b* and Table 5), which indicates that the convection current is increasing. From Table 5, it is also noticed that the x locations remain constant for all the aspect ratios. Figure 15*a* shows the plot of maximum streamfunction versus Rayleigh number for various aspect ratios. It is observed that there is no change in $\psi_{\max}$ up to $\mathrm{Ra} = 10^3$ for all the aspect ratios, because the conduction mode is dominant. As discussed earlier, the contribution of convection supersedes the conduction from $\mathrm{Ra} = 10^3$ onward. Figure 15*b* shows a plot of the value of Nu_l at the midpoint of the bottom wall versus Rayleigh number for various aspect ratios. It is to be noted

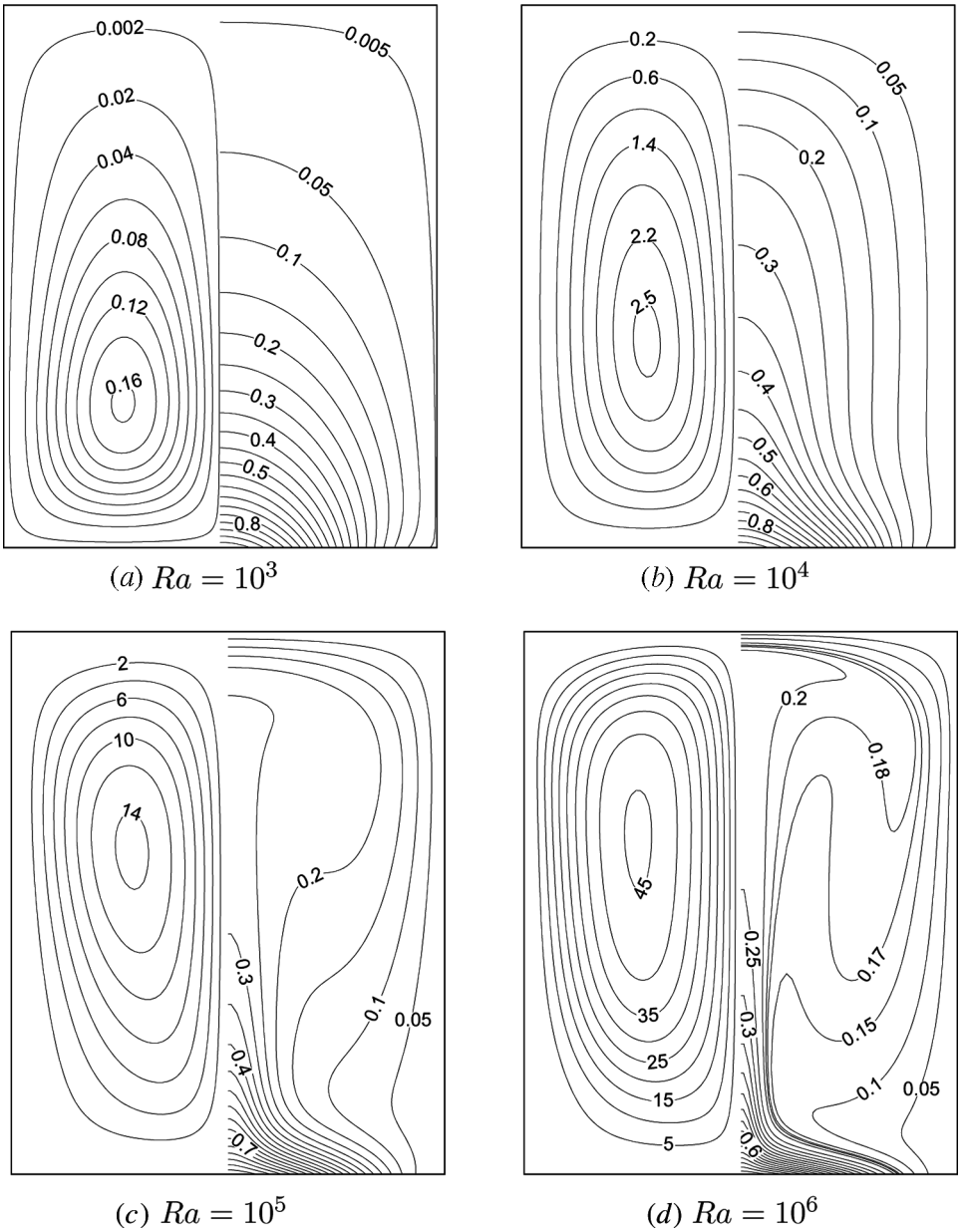

Figure 11. Streamlines and isothermal lines for $A = 1.25$.

that Nu_l decreases from $Ra = 10^3$ to 10^4 and then increases for $Ra = 10^5$–10^6. The same can be seen from Figure 8*b*. This may be due to the readjustment of the isotherms as Ra increases from 10^3 to 10^4. The maximum Nusselt number versus Rayleigh number for various aspect ratios are plotted in Figures 16*a*–16*c*. The

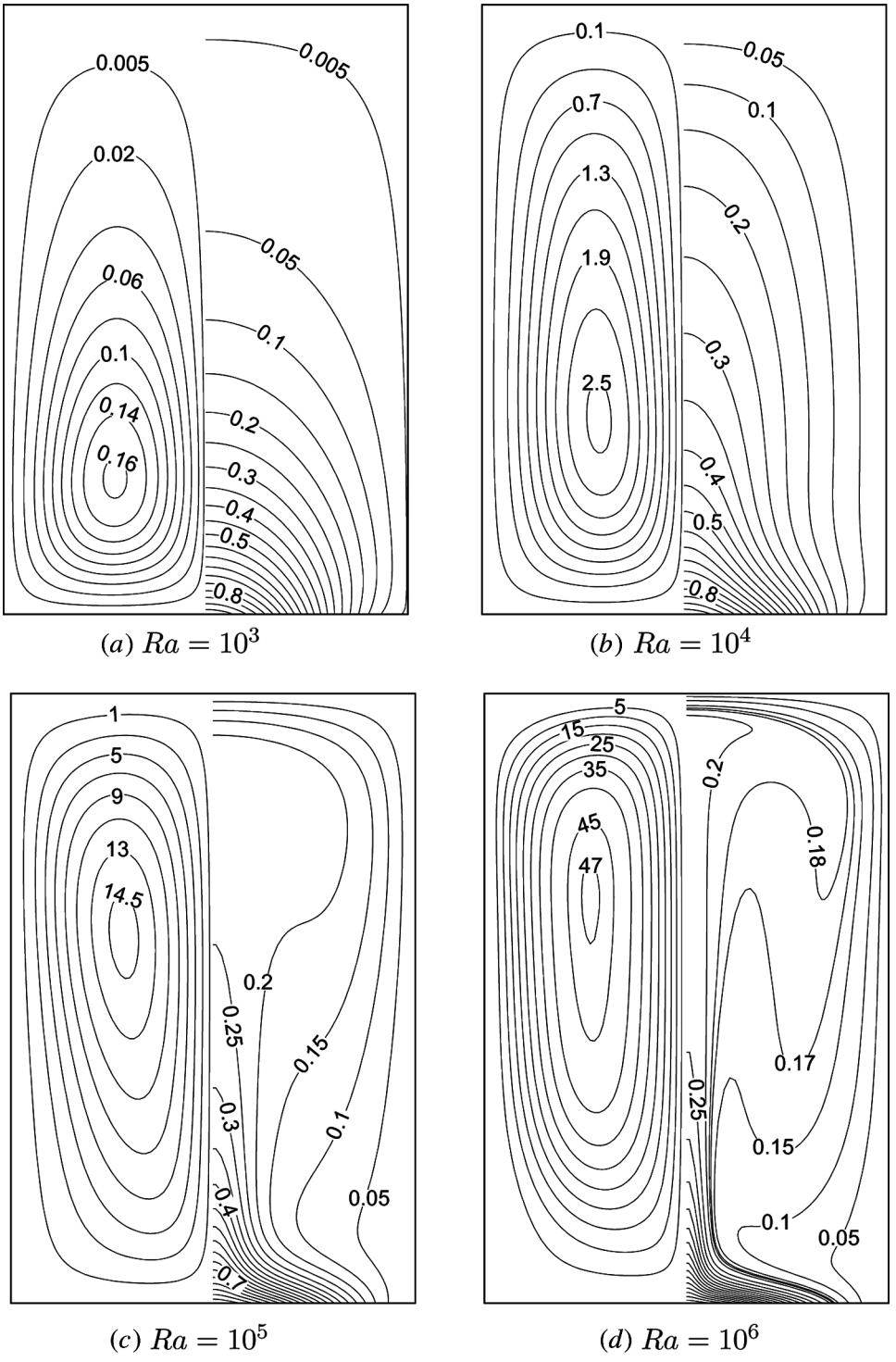

Figure 12. Streamlines and isothermal lines for $A = 1.5$.

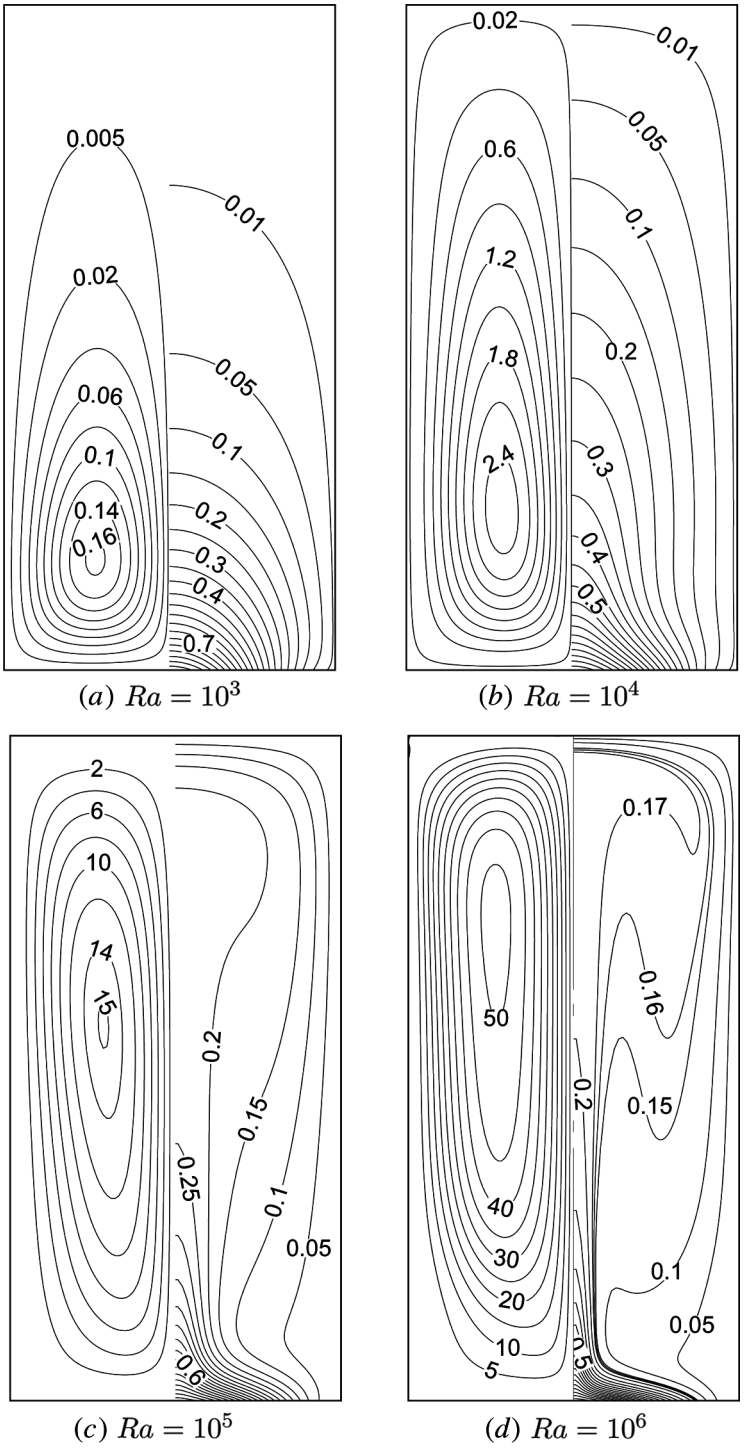

Figure 13. Streamlines and isothermal lines for $A = 2$.

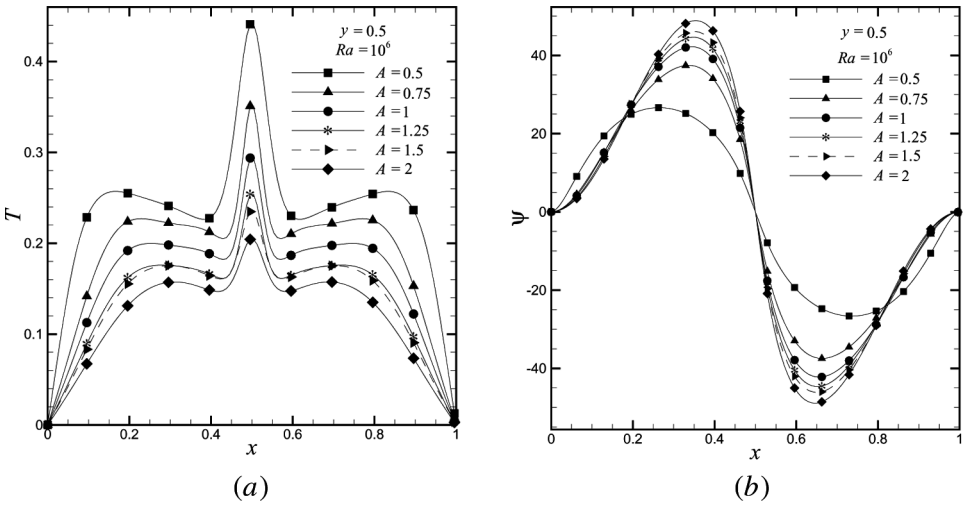

Figure 14. (*a*) Temperature profile. (*b*) Streamfunction profile in horizontal centerline.

absolute Nu_{max} value is the same for all the aspect ratios except $A = 0.5$ for Ra up to 10^3 (Figure 16*a*). In the region $Ra \geq 10^4$, Nu_{max} is greater for the low-aspect-ratio domain.

The case of $A = 0.5$ needs further investigation. The Nu_{max} values for the bottom wall remain unaffected by the aspect ratios (Figure 16*b*). On the top wall, the absolute Nu_{max} value is greater for the lower-aspect-ratio domain (Figure 16*c*). The average Nusselt numbers versus Rayleigh number for various aspect ratios are plotted in Figures 17*a*–17*c*. For the right wall, the absolute Nu_{av} value is higher for the higher-aspect-ratio domain (Figure 17*a*). On the bottom wall, the Nu_{av} value is higher for low aspect ratio. This may be due to the proximity of the top wall to the bottom wall.

CONCLUSIONS

A numerical study has been carried out for natural convection inside a rectangular cavity with sinusoidal temperature boundary condition on the bottom

Table 5. Comparison of ψ_{max} for $Ra = 10^6$

A	ψ_{max}	x	y
0.5	26.658591	0.262500	0.254167
0.75	37.568916	0.264857	0.403559
1	42.572238	0.267396	0.571587
1.25	45.696459	0.264856	0.775484
1.5	47.348841	0.264118	1.004888
2	51.739388	0.263030	1.442267

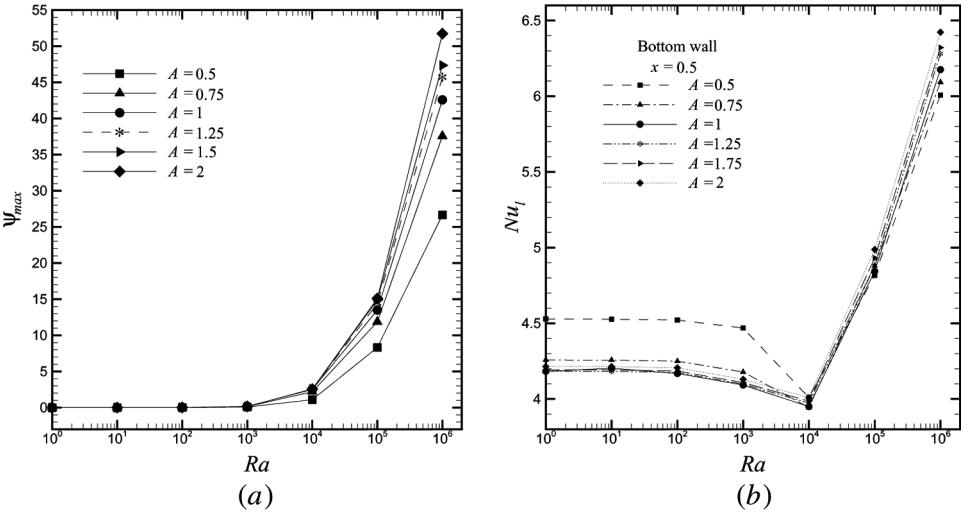

Figure 15. (*a*) Maximum streamfunction distribution for various Ra. (*b*) Local Nusselt number at $x = 0.5$.

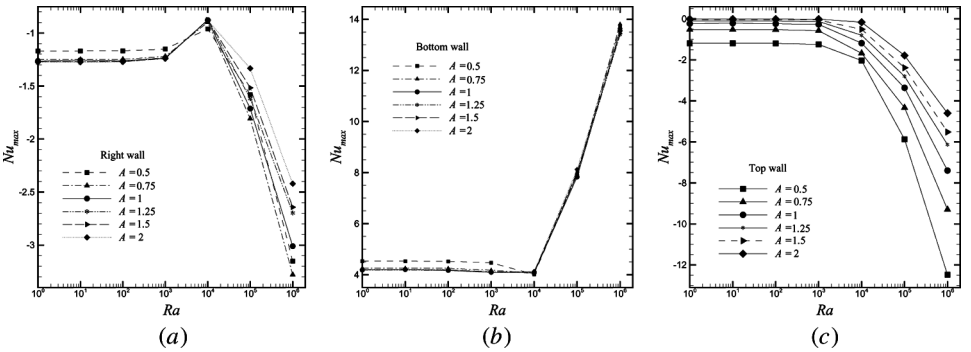

Figure 16. Maximum Nusselt number distribution.

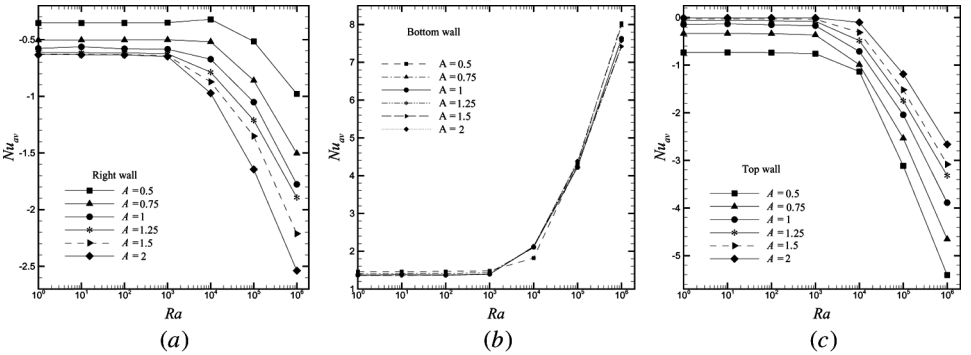

Figure 17. Average Nusselt number distribution.

wall and constant cold temperature boundary condition on other three walls. The following conclusions may be drawn.

For all aspect ratios,

For $\mathrm{Ra} = 10^0 - 10^3$, the heat transfer is dominated by conduction across the fluid layers. When $\mathrm{Ra} \geq 10^4$, the process is dominated by convection.
The flow and heat transfer remains symmetric about the vertical midplane (i.e., $x = 0.5$).

For $A = 1$,

With increase in Ra, maximum T decreases, and the size of the core with relatively uniform temperature increases. $\psi_{\max}$ increases from 0.0 ($\mathrm{Ra} = 10^0$) to 42.6 (for $\mathrm{Ra} = 10^6$).
Nu_l maximum value for the right wall shifts from the bottom to the top as Ra is increased beyond 10^4, due to change in mode from conduction to convection.
For the top wall, the Nu_l maximum occurs at $x = 0.5$, whereas for bottom wall it occurs symmetrically on two cells.

For the range of A considered,

Maximum temperature value decreases with increase in Ra.
$\psi_{\max}$ value increases with increase in A and occurs at the same x location.
$\mathrm{Nu}_{\max}$ and $\mathrm{Nu}_{\mathrm{av}}$ values for the bottom wall are independent of A.
The absolute $\mathrm{Nu}_{\mathrm{av}}$ values on the right wall increase with increase in A.
The absolute $\mathrm{Nu}_{\mathrm{av}}$ values on the top wall decrease with increase in A.
For all cases, change in average Nusselt number and maximum streamfunction up to $\mathrm{Ra} = 10^3$ is very small.

REFERENCES

1. S. Ostrach, Natural Convection in Enclosures, *J. Heat Transfer*, 50th Anniversary Issue, vol. 110, no. 4–B, pp. 1175–1190, 1988.
2. P. H. Oosthuizen, Natural Convective Heat Transfer across a Cavity with Cooled Top Surface Application to a Simple Dryer, *Proc. ASME Heat Transfer Division, Single and Multiphase Convective Heat Transfer*, vol. 145, pp. 1–11, 1990.
3. P. H. Oosthuizen and P. F. Monaghan, Free Convective Flow in a Vertical Non–rectangular Cavity with a Cooled Flat Upper Surface, Natural/Forced Convection and Combustion Simulation, *Proc. 2nd International Conference on Advanced Computational Methods in Heat Transfer*, vol. 2, Milan, pp. 192–208, 1992.
4. P. H. Oosthuizen, Free Convective Flow in an Enclosure with a Cooled Inclined Upper Surface, *Comput. Mech.*, vol. 14, pp. 420–430, 1994.
5. M. M. Ganzarolli and L. F. Milanez, Natural Convection in Rectangular Enclosures Heated from Below and Symmetrically Cooled from the Sides, *Int. J. Heat Mass Transfer*, vol. 38, pp. 1063–1073, 1995.
6. W. Chmaissem and D. Daguenet, Numerical Study of the Natural Convection of Boussinesq Equations in Parallelepipedal Cavities with Isothermal Walls and Heated from

Two Sides: Influence of Wall Conditions, *Energy Conversion Management*, vol. 40, pp. 1041–1056, 1999.
7. A. Kumar, M. F. Baig, and W. Asrar, Evolution to Chaotic Natural Convection in a Rectangular Enclosure with Mixed Boundary Conditions, *Numer. Heat Transfer A*, vol. 34, pp. 447–462, 1998.
8. O. Aydin, A. Ünal, and T. Ayhan, Natural Convection in Rectangular Enclosures Heated from One Side and Cooled from the Ceiling, *Int. J. Heat Mass Transfer*, vol. 42, pp. 2345–2355, 1999.
9. I. Sezai and A. A. Mohamad, Natural Convection in a Rectangular Cavity Heated from Below and Cooled from Top as well as the Sides, *Phys. Fluids*, vol. 12, no. 2, pp. 432–443, 2000.
10. I. E. Sarris, I. Lekakis, and N. S. Vlachos, Natural Convection in a 2D Enclosure with Sinusoidal Upper Wall Temperature, *Numer. Heat Transfer A*, vol. 42, pp. 513–530, 2002.
11. A. Dalal and M. K. Das, Laminar Natural Convection in a Complicated Cavity with Spatially Variable Upper Wall Temperature, *Proc. 2003 ASME Summer Heat Transfer Conf.*, Las Vegas, NV, 2003.
12. A. Dalal and M. K. Das, Laminar Natural Convection in an Inclined Complicated Cavity with Spatially Variable Wall Temperature, *Int. J. Heat Mass Transfer*, vol. 48, pp. 3833–3854, 2005.
13. C. R. Maliska and G. D. Raithby, A Method for Computing Three Dimensional Flows Using Non-orthogonal Boundary-Fitted Co-ordinates, *Int. J. Numer. Meth. Fluids*, vol. 4, pp. 519–537, 1984.
14. M. N. Özisik, *Finite Difference Methods in Heat Transfer*, CRC Press, London, UK, 1994.
15. J. F. Thompson, Z. U. A. Warsi, and C. W. Mastin, *Numerical Grid Generation*, North Holland, Amsterdam, 1985.
16. A. Dalal, Computation of Two-Dimensional Incompressible Laminar Flow and Heat Transfer in Complex Boundaries Using Finite-Volume Method, M.Tech. thesis, Indian Institute of Technology Guwahati, Guwahati, India, 2003.
17. S. V. Patankar, *Numerical Heat Transfer and Fluid Flow*, Hemisphere, New York, 1980.
18. T. Hayase, J. C. Humphrey, and R. Greif, A Consistently Formulated QUICK Scheme for Fast and Stable Convergence Using Finite-Volume Iterative Calculation Procedures, *J. Comput. Phys.*, vol. 98, pp. 180–118, 1992.
19. H. K. Versteeg and W. Malalasekera, *An Introduction to Computational Fluid Dynamics, The Finite Volume Method*, Longman Group, England, 1995.
20. J. P. Van Doormall and G. D. Raithby, Enhancements of the SIMPLE Method for Predicting Incompressible Fluid Flows, *Numer. Heat Transfer*, vol. 7, pp. 147–163, 1984.
21. G. de Vahl Davis, Natural Convection of Air in a Square Cavity: A Benchmark Numerical Solution, *Int. J. Numer. Meth. Fluids*, vol. 3, pp. 249–264, 1983.
22. N. C. Markatos and K. A. Perikleous, Laminar and Turbulent Natural Convection in an Enclosed Cavity, *Int. J. Heat Mass Transfer*, vol. 27, no. 5, pp. 755–772, 1984.
23. G. V. Hadjisophocleous, A. C. M. Sousa, and J. E. S. Venart, Prediction of Transient Natural Convection in Enclosures of Arbitrary Geometry Using a Nonorthogonal Numerical Model, *Numer. Heat Transfer*, vol. 13, pp. 373–392, 1988.